A mass abrasion model with the melting and cutting mechanisms during high-speed projectile penetration into concrete slabs

Jianguo Ning[1], Huilan Ren[1], Zhao Li[2], and Xiangzhao Xu[1*]

[1] *State Key Laboratory of Explosion Science and Technology, Beijing Institute of Technology, Beijing 100081, China;*
[2] *China North Vehicle Research Institute, Beijing 100072, China*

In this study, ogive-nose projectile penetration into concrete slabs was tested at initial projectile impact velocities ranging from 1325.0 m/s to 1425.0 m/s. The depth of penetration and mass loss of the projectiles were measured, and the residual projectiles were recovered after the penetration tests. Scanning electron microscopy and metallographic microscopy of the microstructures were performed on various sections and outer surfaces of the projectiles taken from different locations of the residual projectiles, to analyze the intrinsic mechanisms of mass abrasion. The analysis results reveal that, during high-speed projectile penetration, projectile abrasion is caused by multiple mechanisms. Based on the cavity expansion theory, a projectile penetration model was established by considering the two main mass loss mechanisms observed in the microscopic tests. The theoretical predictions of the penetration depth, mass loss rate, and change of projectile head are consistent with the experimental results obtained both in this study and previous research.

Projectile abrasion, Microscopic observation, High-speed penetration, Concrete target

1.   Introduction

Concrete is a ubiquitous material used in both industry and military establishments. The penetration of a projectile into concrete has attracted considerable research attention [1-8]. Previous studies [9,10], have defined low-speed penetration as ranging between 300 and 800 m/s, and high-speed penetration between 800 and 1500 m/s. Furthermore, low-speed penetration into concrete targets has been studied extensively. By assuming a rigid projectile, Forrestal et al. [10,11] proposed a widely used semi-empirical formula, whose predictions are consistent with experimental data. However, many previous experiments [10,12-18] have indicated that projectile abrasion becomes significant at high impact velocities, which considerably affects the penetration efficiency. Furthermore, severe projectile abrasion even affects the stability of a ballistic trajectory and may result in the

structural failure of the projectiles [19]. Hence, the assumption of rigid projectile is inappropriate during high-speed penetration because of projectile abrasion. There is, therefore, a need to further investigate the projectile abrasion mechanism at high impact velocities.

Extensive experimental studies have provided detailed insight into the projectile abrasion mechanisms during the penetration process [14,20-26]. Forrestal et al. [10,20,27] observed considerable mass abrasion was considerable at the nose of projectiles during high-velocity penetration. An initial impact velocity exceeding 1200.0 m/s may result in a mass loss of the projectile of up to 7.0%. Silling and Forrestal [23] proposed an empirical relation between the initial kinetic energy of a projectile and the mass loss rate based on six sets of penetration tests. However, obtaining real-time experimental data on projectile abrasion during the instantaneous penetration process is imperative. Therefore, developing an appropriate experimental method is imperative for investigating projectile abrasion. Recent studies

---

have indicated that the microscopic analysis of residual projectiles can reveal mass loss mechanisms. Zhang et al. [12] observed the heat affect zone (HAZ) and adiabatic shear bands on the surface of a recovered projectile. They speculated that the mass loss of projectiles could be attributed to the shear cracks preceded by adiabatic shear bands. Guo et al. [14] performed optical microscopy, energy dispersive X-ray (EDX) detection, and microhardness testing on residual projectiles recovered after penetration into concrete slabs (derived from the nose, shank, and tail) to examine their mesostructures. Their results revealed that thermal softening and material flow are the main mechanisms underlying projectile mass abrasion. He et al. [15] performed two-group penetration tests on a concept projectile for high-speed penetration (CPHP) with impact velocities ranging from 1130.0 m/s to 1650.0 m/s. They observed the HAZ caused by thermal melting on the projectile surface through metallographic observation. Their results revealed that the main cause of mass loss was the peeling of the molten surface layer. Furthermore, several narrow white bands, caused by adiabatic shear, were observed in the CPHP nose tip. These bands had minor contribution to mass loss. Similarly, Feng et al. [28] revealed the presence of adiabatic shear bands on a damaged 30CrMnSiNi2A steel projectile nose. In addition to the HAZ, Wu et al. [16] observed numerous deep groove cuts caused by aggregates and hard particles in a concrete target on the surface of residual projectiles made of various materials.

Despite extensive experimental analyses of projectile mass abrasion, our accurate and unified understanding of the microscopic observations of the projectile head and of the essential mechanism of projectile abrasion remains incomplete. Experimental studies at the microscopic scale have either focused on the individual locations of residual projectiles using scanning electron microscopy (SEM) images (Guo et al. [14,29]) or have relied on a single experimental method (He et al. [15,30]). Furthermore, most published theoretical studies based on theoretical analysis typically exhibit the following two characteristics. First, studies such as those by Silling and Forrestal [23], He et al. [30], Yang et al. [31], and Wen et al. [32] have presented an engineering model based on the empirical parameters, which were either fitted from experimental data or obtained from experimental rules. Second, studies such as those by Jones et al. [21], Guo et al. [24], and He et al. [33] have investigated the abrasion mechanism and proposed an analysis model based on a single abrasion mechanism. However, do not envisage mass abrasion as resulting from the interaction of multiple mechanisms. This motivates the need to investigate abrasion mechanisms through a systematic microscopic analysis of residual projectiles.

In this study, four sets of experiments on projectile penetration into concrete targets were conducted with initial impact velocities ranging from 1325.0 to 1425.0 m/s. The residual projectiles were recovered, and microscopic analyses were performed on their noses to investigate the abrasion mechanism during high-speed penetration. Several mass abrasion locations were defined on the projectile nose, and the microstructures of the cross section and surface of those locations were observed by SEM and with a metallographic microscope. These observations reveal that the mass abrasion of projectile is caused not by a single mechanism, but by multiple mechanisms. Next, based on the cavity expansion theory, a projectile penetration model was established by considering the two main mass loss mechanisms observed in the microscopic tests: thermal melting and cutting. According to the model, these effects are coupled and influenced each other, contributing to the total mass loss of the projectile. The theoretical predictions of the penetration depth, mass loss rate, and the change of projectile head are consistent with the test data obtained within this study and others published reports.

2. High-speed penetration experiments

2.1 Projectile and concrete target

The ogive-nose projectiles used in this study were made of PCrNi3MoV steel with a yield strength of 835.0 MPa. The total length L_p, radius a, density ρ_p and initial mass M_0 of the projectiles were 197.5 mm, 50.0 mm, 7850.0 kg/m^3, and 5.7 kg, respectively. Their aspect ratio of was defined as $L_p/2a = 1.975$. The caliber-radius-head (CRH) of the projectile nose was $\psi = 1.2$. The geometry of the projectile and its characteristic parameters are illustrated in Fig. 1.

All the concrete slabs were made from the same batch of concrete, and were cured for 28 days under the same curing condition. The size of the concrete targets was 2.0 m × 2.0 m × 1.75 m (penetration direction). Thus, they were sufficiently thick to function as semi-infinite slabs. The density ρ_t and unconfined compressive strength f_c of the concrete slabs were 2300.0 kg/m^3 and 50.0 MPa, respectively.

2.2 Experimental layout

A 100.0 mm caliber smoothbore gun was used to launch the 5.7 kg projectiles to penetrate the concrete targets, and the flying distance of the projectiles was 10.0 m. The speed-measurement system included a high-speed camera system and a white background board placed to the side, 4.0 m away from the concrete target. The initial projectile impact velocity was measured by evaluating photographs from the high-speed camera system, which measures and records the flight attitude and the interaction between the projectile and the front surface of the target.
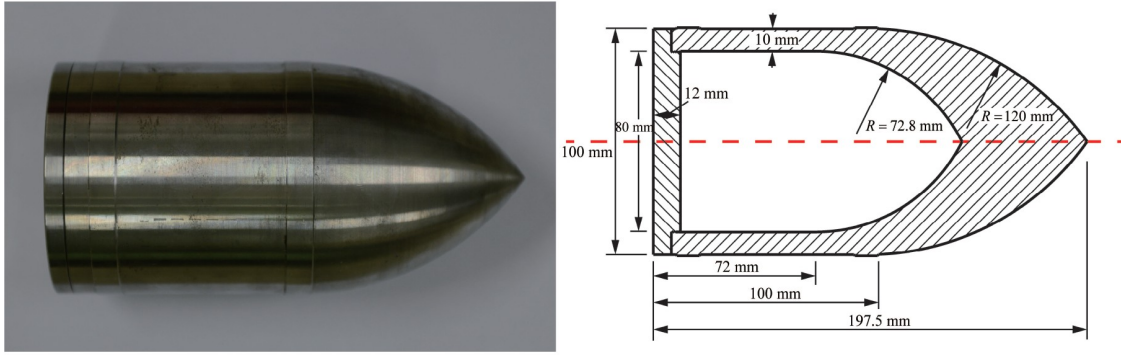
Figure 1 Schematic diagram of projectile size.

2.3 Experiment results

We conducted four sets of tests on high-speed projectile penetration into concrete slabs. As displayed in Fig. 2a, the flying and impact gesture of the projectiles is approximately normal. The initial projectile parameters are listed in Table 1. After penetration, the residual projectiles were carefully recovered, and some parameters of the residual projectiles, such as their residual mass M_{pr} and residual length L_{pr}, were

Figure 2 Experimental results. **a** Flight attitude and penetration process recorded by high-speed camera system for tests 1-4. **b** Comparison of shape variation of projectiles before and after penetration.

measured, as presented in Table 1.

Table 1 indicates that, as the initial impact velocity increases, the final penetration depth of projectile (DOP) also increases, whereas the remaining projectile mass decreases. Figure 2b shows the residual shape of the projectile after penetrating the concrete slab at initial impact velocities of 1325.0, 1385.0, 1386.0, and 1425.0 m/s, respectively. Clearly, considerable mass loss and nose blunting occur at the projectile noses. None of the projectiles in the four sets of penetration experiments penetrated through the concrete target.
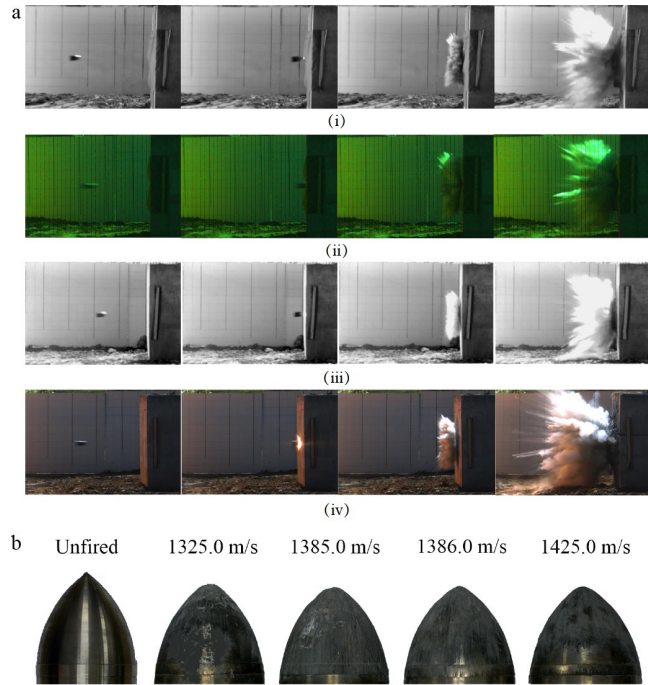
3. Metallographic analysis of residual projectiles

According to Refs. [34,35], mass abrasion occurs mainly at the projectile nose. Therefore, the samples were obtained at various positions on the residual projectile nose. The sample size was 10.0 mm × 8.0 mm × 5.0 mm, including the cross sections, longitudinal sections, and outer surface of the metallographic samples.

3.1 Sample preparation

After performing the experimental penetration tests, we recovered the residual projectiles and cleaned them to obtain a clear surface structure. Firstly, the residual projectiles were sectioned along their axis. Some specimens were cut from the residual projectiles from five typical locations for microscopic analysis. An S-4800 SEM (HITACHI, Japan) was used to observe the microscopic structure and composition of

Table 1 Experiment results

Case No.	M_0 (kg)	L_p (mm)	V_s (m/s)	f_c (MPa)	DOP (m)	L_{pr} (mm)	M_{pr} (mm)
Test-1	5.734	197.5	1325.0	50.0	0.74	181.3	5.35
Test-2	5.700	197.5	1385.0	50.0	0.82	178.9	5.31
Test-3	5.778	197.5	1386.0	50.0	0.70	181.5	5.33
Test-4	5.720	197.5	1425.0	50.0	0.86	178.3	5.21

the sample surfaces. Figure 3 shows the original microstructure of a PCrNi3MoV steel projectile. The tempered sorbite structure was the main microstructure, showing considerable carbide precipitation. This microstructure accounts for the high strength and outstanding ductility of this material. Table 2 also lists the chemical composition of PCrNi3MoV.

Figure 4b shows typical SEM photographs of the longitudinal section at various locations on the residual projectile nose. These microscopic observations reveal distinct morphologies: the microstructure inside the recovered projectile is consistent with that of the projectile before penetration and is not affected by frictional heat. This region is called the matrix region. However, the microstructure near the projectile surface clearly differs considerably from that in the matrix region. Specifically, the microstructure of the outer region becomes dense and is called the dense layer. This layer was approximately 30.0 μm thick at a certain area near the nose tip and approximately 10.0 μm thick at a certain area close to the bourrelet. Thus, the dense layer thickness on the surface of the remaining longitudinal section of the projectile decreased with the observation point away from the projectile tip.

3.2 Microscopic observation

Optical metallographic microscopy was performed on a small specimen extracted from the projectile surface. Figure 4a shows the 20× and 100× magnified metallographic images of the specimen. A solidified molten material flow pattern of concrete was observed on most of the projectile surfaces. Only a small part of the projectile surface was bare metal. Many long and deep grooves were observed on the bare metal surface. Detailed features of the grooves are displayed in the magnified regions (red boxes). The groove surfaces were very rough, and the grooves had a variable width.
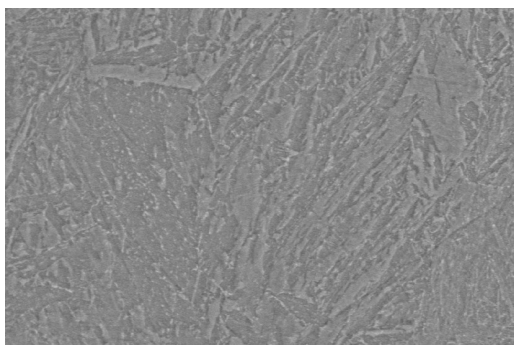
The SEM microstructure of the cross section of the recovered projectile at various observation points is shown in Fig. 4c. The magnification in Fig. 4c is lower than that in Fig. 4b, and the edge profile of the cross section of the projectile can be observed on a larger scale. As shown in Fig. 4c, unlike the smooth edge profile of the longitudinal section of the projectile nose, the surface profile of the projectile body is serrated. It features numerous closely packed parallel V-shaped edge profiles. Combining the metallographic images of the residual projectile recorded in Fig. 4a, these V-shaped edge profiles can be regarded as grooves cross sections on the projectile nose surface. These groove depths are gen-
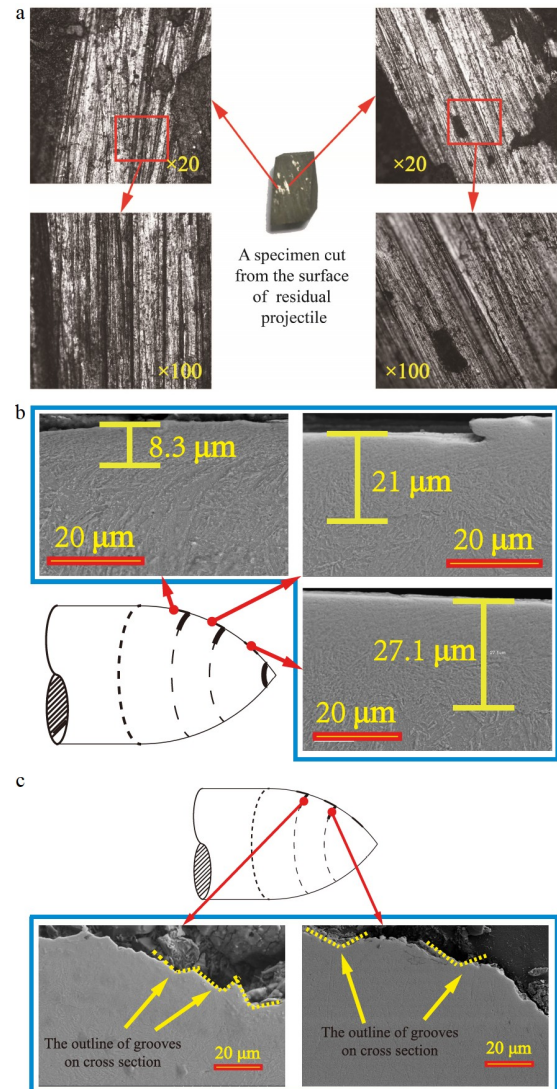

Figure 4 Microscopic observation results. **a** Metallograph of sample from projectile's outer surface. **b** SEM photograph of longitudinal section of projectile nose from different locations. **c** SEM photograph of cross section of projectile nose from different locations.

Figure 3 SEM image showing initial microstructure of the projectile.

Table 2 Chemical composition of PCrNi3MoV (wt.%)

	C	Si	Mn	P	S	Cr	Ni	Mo	V
PCrNi3MoV	0.32	0.27	0.35	≤ 0.025	≤ 0.025	1.2-1.5	3.0-3.5	0.35-0.45	0.10-0.25

erally between 10.0 μm and 20.0 μm, and some deep grooves even affect the thickness of the HAZ. Furthermore, higher deposits are formed on both sides of the grooves, which is a typical indicator of abrasive wear. The hard aggregates in the concrete target cut the soft metal material on the surface of projectile continuously during the penetration process, resulting in mass loss and nose blunting.

These microscopic observations on the residual projectiles illustrate the complexity of projectile abrasion during high-speed penetration. A dense layer was observed, which differed from the matrix region inside the projectile. Numerous long parallel grooves on the projectile surface were also apparent. Complex morphologies, such as randomly distributed microcracks and a broken external profile caused by the peeling of projectile material, were also observed. These results suggest that projectile mass abrasion is caused by the coupling of multiple mechanisms.

3.3 EDX analysis

A surface layer specimen of the recovered projectile was placed on an aluminum plate, and its two regions were analyzed, as shown in Fig. 5. The upper part of Fig. 5 shows the typical longitudinal section microstructure of the surface of the projectile body and its magnification. Region 1 is

located outside the surface of the missile body, and Region 2 is located in the dense area on the missile body surface. The EDX detector in the J-4800 SEM was used to characterize the compositions of the two regions. Considering various elements (including C, Si, and Fe), further analysis of the two regions was conducted by EDX. The results are displayed at the bottom of Fig. 5, and specific values are listed in Table 3.

The Fe content was almost null on the recovered projectile surface (e.g., Region 1), and only Si, C, and O were present. This supports the hypothesis that the recovered projectile surface was composed of melted projectile material and sand or stone particles. However, in the dense area below the projectile surface, the Fe content increased sharply, and the Si and C contents decreased sharply. This indicates that no concrete particles, sand aggregate, or other impurities existed in the dense area.

3.4 Abrasion mechanisms

A denser layer formed on the projectile surface, which differed from the internal matrix region. The previous study [36] has revealed that the intense heat generated by the considerable sliding friction between the projectile and the target during high-speed penetration can produce a phase transition in the projectile material. Three specimens were
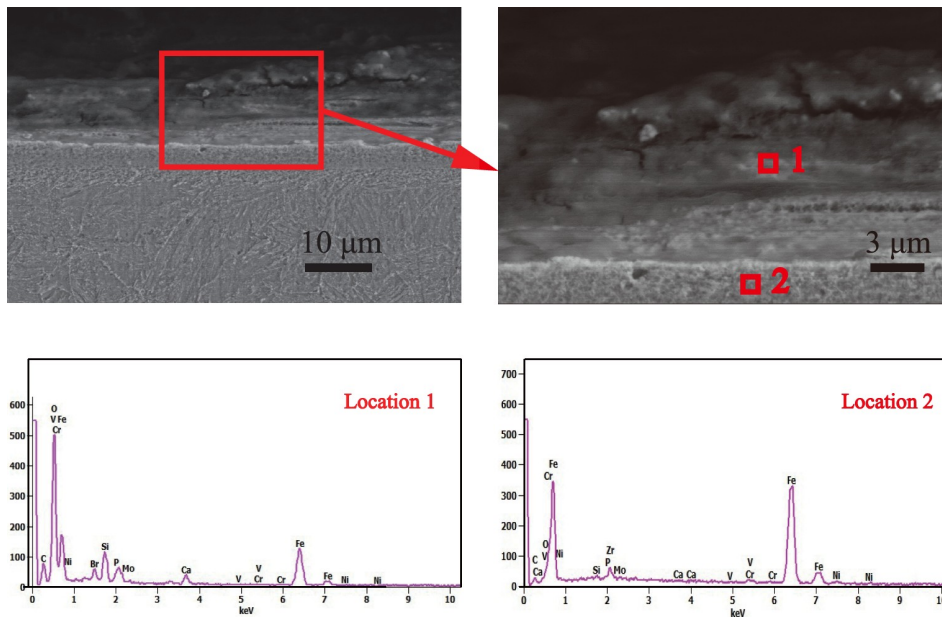

Figure 5 EDX image.

Table 3 EDX results

Region	C	O	Si	Ca	Fe
Region 1 (wt.%)	19.60	37.64	4.92	1.81	30.58
Region 2 (wt.%)	0	1.27	0.26	0.10	90.34
Region 1 (at.%)	33.67	48.53	3.62	0.93	11.30
Region 2 (at.%)	0	4.37	0.51	0.14	88.74

prepared for comparative microstructure analysis to investigate whether the formation of the dense layer is related to a high temperature. The first specimen was sectioned from the unfired original projectile, and the second specimen was sectioned from the residual projectile surface material. The third specimen was sectioned from the original projectile material, heated to 1673.0 K for 10.0 s. Figure 6 shows the SEM microstructures of the three specimens from left to right, respectively. For convenience, the dense layer and matrix region are defined as zone Ⅰ and zone Ⅱ. The zone exhibited a similar microstructure to that of the original projectile. In contrast to the original projectile material, the microstructure of the specimen exposed to a high temperature exhibited cementite precipitation and cementite coalescence. In particular, the heat-treated specimen exhibited a microstructure similar to that of zone Ⅰ, which strongly supports the hypothesis that the metal material on the projectile surface is affected by high temperatures. Generally, the dense layer is called the HAZ. This result is consistent with the metallographic microscope results of Guo et al. [14] and He et al. [15] on the HAZ.

The peeling of the projectile surface material caused by thermal melting is not the only mechanism for projectile abrasion. Metallographic observations of the projectile surface and SEM observation of the longitudinal and cross sections of the recovered projectile have identified numerous horizontal grooves on the nose of the recovered projectile. Under static conditions, adamant particles (for instance, aggregates) are no harder than the material of the projectile (e.g., high-strength steel), and forming numerous grooves on the projectile surface by cutting is difficult. During high-speed penetration, the surface temperature of the projectile

Figure 6   SEM photograph of sample from different specimens.

increases, which reduces the strength of the projectile surface material. Even a portion of the material on the projectile surface loses its strength because of melting. Furthermore, the projectile is subjected to strong resistance from the concrete target during penetration. Its surface material, softened by friction heat, constantly encounters hard particles that are unaffected by the high temperature. These hard particles become pressed into the projectile surface under a high pressure from the concrete target. Generally, the projectile body surface is continuously cut by hard particles such as aggregates, which results in the formation of numerous grooves all over the projectile nose. The above analysis revealed that cutting by hard particles, such as aggregates, is an essential mechanism of projectile abrasion.

The above microstructural analysis of the residual projectile identified two abrasion phenomena through SEM and metallographic microscopy. The continuous distribution of the HAZ revealed that the peeling of the projectile surface material caused by thermal melting results in mass loss. Numerous deep and long grooves on the projectile nose surface indicate that cutting by aggregates is also a major abrasion mechanism during high-speed penetration. Therefore, both thermal melting and cutting phenomena exist simultaneously during penetration. In a word, the mass abrasion of projectiles is complex and is caused by the coupling effect of multiple mechanisms.

4. Penetration model considering mass abrasion

4.1 Cavity expansion theory

The cavity expansion theory is typically used to calculate projectile penetration resistance. The Johnon-Holmquist-Cook (HJC) model, widely used for geological materials such as concrete [37,38], accurately describes the void compaction of concrete subjected to high pressures and permanent densification on occurrence of failure. Furthermore, a high hydrostatic pressure may lead to the pore failure of concrete material, which may in turn result in volume yield. The Drucker-Prager Cap failure criterion describes this compaction phenomenon in concrete. It mainly considers the end of the Drucker-Prager shear plane and an elliptical "cap" reinforcing surface.

Firstly, the specific form of the equation of state is introduced as follows:

$$p = \begin{cases} K_e\mu, & p < p_c, \\ p_c + K_c(\mu - \mu_c), & p_c p < p_l, \\ K_1\overline{\mu} + K_2\overline{\mu}^2 + K_3\overline{\mu}^3, & p > p_l, \end{cases} \tag{1}$$

where $\mu = \rho/(\rho_0 - 1)$ is the volumetric strain for the initial and current density ρ_0, and ρ; and K_e, K_c, K_1, K_2, and K_3 are material parameters, and the expressions for K_c and $\overline{\mu}$ are
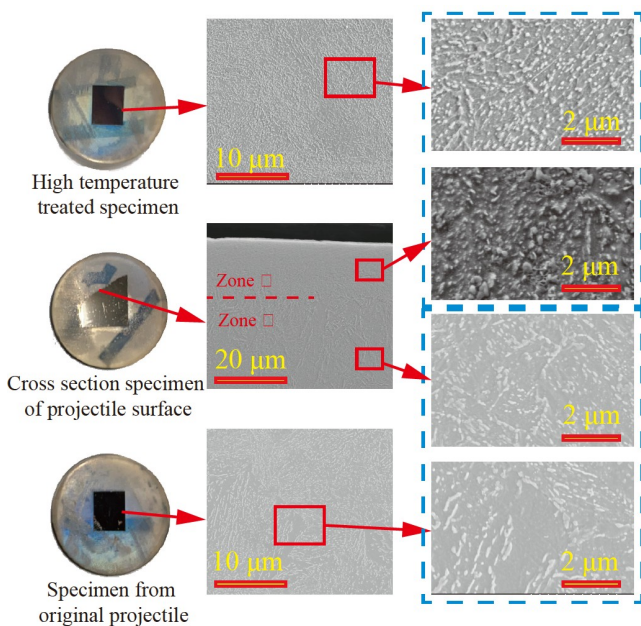
given by

$$K_c = \frac{p_l - p_c}{\mu_l - \mu_c}, \tag{2}$$

$$\overline{\mu} = \frac{\mu - \mu_l}{1 + \mu_l}, \tag{3}$$

where p_c and p_l are the pressure at μ_c and μ_l, respectively.

The following equation is the specific expression of the Drucker-Prager Cap failure criterion. The Drucker-Prager shear plane is described by

$$q - p\tan\beta = \tau_0, \ p < p_m, \tag{4}$$

where p is the hydrostatic pressure, β is the material friction angle, τ_0 is the cohesive strength, and $q = \sigma_r - \sigma_\theta$ is the Mises stress.

The strengthening surface F_c of "cap" can be expressed as follows:

$$F_c = \sqrt{(p - p_m)^2 + (Rq)^2} - R\tau_m, \tag{5}$$

where τ_m is the peak shear strength and p_m is the hydrostatic pressure, and R is the parameter that controls the shape of the "cap".

Figure 7 compares the prediction of the adopted model and test data available in the literature. The parameter values of HJC model and Drucker-Prager Cap failure criterion are not discussed in this manuscript, but mainly refer to classical literature [39]. Concrete is mainly subjected to high pressure and high strain during high speed penetration of projectile.
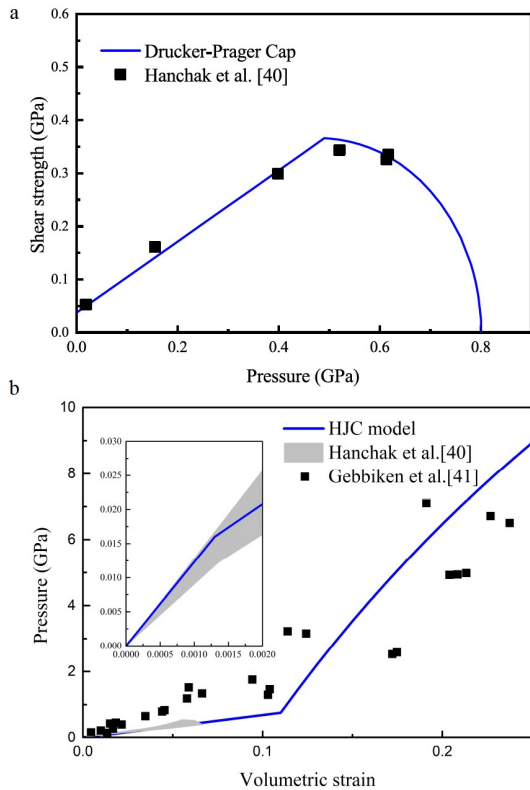

Figure 7 Comparison between the prediction results and the test data [40,41]. **a** Yield criterion, **b** HJC model.

As shown in Fig. 7b, the predictions of HJC model are in good agreement with multiple sets of experimental data. In summary, the adopted model accurately describes the material constitutive behavior of concrete.

4.2 Coupled abrasion model

Previously proposed abrasion models predominantly considered single abrasion mechanisms. For example, Jones et al. [21] and Davis et al. [36] proposed a theoretical model for mass abrasion based on the assumption that the heat whole produced by the friction between the projectile surface and the slab produces projectile surface abrasion. Guo et al. [29] also believed that the aggregates can cut the projectile material during the penetration process and proposed a novel abrasion model according to the Archard model. However, single abrasion mechanism cannot reflect the real process of projectile abrasion during penetration. According to the microscopic observation in this study, a molten layer and a high number of grooves exist simultaneously, which indicates that thermal melting and cutting by aggregates are coupled phenomena. Therefore, we propose a coupled model to analyze the entire penetration process and the phenomenon of mass loss. The model is based on the following premises:

(1) The penetration trajectory remains straight (i.e., without deflections) until the projectile comes to a stop.

(2) Both the projectile and the target material conform to the assumptions of continuum mechanics, and the thermal parameters of the projectile remain constant during the penetration process.

(3) According to Ref. [35], the proportion of mass loss of the shank relative to the total mass loss is considerably low. Thus, we assume that mass abrasion occurs only at the projectile nose.

(4) The process of penetration into a semi-finite target involves two stages: the crater region ($t_0 < t < t_1$) and the tunnel region ($t_1 < t < t_e$) [42,43]. The projectile is assumed to be a rigid body that does not experience mass loss in the crater region.

Owing to the symmetry of the ogival projectile, we considered one half of the two-dimensional section of the projectile as the analysis object. A spatial mesh of the object was constructed, and the penetration process was discretized into multiple time steps. In each time step, the mass loss of the projectile body was considered to have contributions both from melting and from being cut by aggregates.

First, the two-dimensional heat conduction equation was established to calculate the temperature distributions over the entire sections of the projectile.

$$\rho_p c_p \frac{\partial T}{\partial t} = \lambda \left(\frac{\partial^2 T}{\partial x^2} + \frac{\partial^2 T}{\partial y^2} \right), \tag{6}$$

where x and y are horizontal and vertical coordinates of the grid, respectively; ρ_p is the projectile density; c_p and λ are heat capacity and thermal conductivity, respectively. The alternating direction implicit method was used to calculate the temperature distribution at the grid nodes, and the temperature at any point at the center of the grids was obtained by the interpolation method. Then, the magnitude of mass loss due to melting was obtained.

$$\Delta E_m = h_m dA_s, \tag{7}$$

where h_m is the depth of the molten layer on the projectile surface, dA_s is the unit area of the projectile nose.

Second, the material on the projectile surface softens or even melts because of friction heat. Concurrently, the aggregates or other hard particles between the concrete and the projectile are subjected to a maximum pressure according to the dynamic cavity expansion theory. Furthermore, metallographic images of the projectile outer surface reveal many long and deep grooves were observed on the surface of the bare metal, with deposits caused by compression on both sides of these grooves. This phenomenon is consistent with the description of the Rabinowicz wear theory [44]. The mass loss caused by the cutting mechanism was therefore calculated according to the Rabinowicz wear theory. A previous study observed an approximately linear relationship between the hardness and the yield strength of the metal [45]. Furthermore, to highlight the effect of the projectile yield strength on mass abrasion more clearly, the hardness of the projectile material was replaced with its yield strength in the calculations. The volume of the projectile cut by hard aggregates per unit area in a certain time step can be expressed as

$$\Delta E_c = NK \frac{pv_r(t)}{H} = Z \frac{pv_r(t)}{\sigma_y(t)}, \tag{8}$$

where p is the stress acting on the projectile surface, v_r is the relative velocity between the projectile and the target and is obtained from the geometric positions, K is the Rabinowicz parameter that represents the average tangent of the abrasive particles, and N is the number of grooves per unit area on the outer surface of the projectile. H and σ_y are the hardness and dynamic yield stress of the projectile, respectively. Z is the parameter that integrates the ratio of hardness to yield strength and the parameters K and N. In this study, Z was assumed to be constant under certain experimental conditions. According to the Johnson-Cook model [46], the dynamic yield stress of the projectile metal can be expressed as a function of temperature T as

$$\sigma_y = \sigma \left[1 + C\ln\left(\frac{\dot\varepsilon}{\dot\varepsilon_0}\right) \right]\left[1 - \left(\frac{T-T_0}{T_m-T_0}\right)^m \right], \tag{9}$$

where σ_y is Mieses flow stress, ε is the accumulated equivalent plastic strain, T_m is the melting point, T_0 is room temperature, $\dot\varepsilon$ is plastic strain rate, $\dot\varepsilon = 1/s$ is the reference plastic strain rate, and σ is the yield strength at the reference strain rate. Other material constants, such as C and m, were measured experimentally [47]. Based on the microscopic observation mentioned above, the groove depth is approximately 10-30 μm. For the convenience of the calculation and the temperature limit of the application of the Johnson-Cook constitutive equation, T is uniform 20 μm below the projectile surface. Herein, we approximated the properties of the steel projectile by using the properties of its major constituent Fe.

Thus, the normal regression volume per unit area dS on the projectile surface in time step dt is $\Delta E = \Delta E_m + \Delta E_s$. In particular, the nose profile is divided into a sufficiently large number of nodes to simulate its evolution. The nodes recede along the normal direction because of mass abrasion, and the receding distance of each node can be calculated using Eqs. (4) and (5). The updated nodes represent the nose profile at the start of the next time step. The evolution of the projectile nose was obtained in a similar fashion and integrated with respect to the penetration time until the penetration process was complete. The total mass loss of the projectile during penetration is expressed as

$$E_{total} = \int_{t_1}^{t_e} \left[Z\frac{pv_r(t)}{\sigma_y(t)} + h_m dA_s \right] dt. \tag{10}$$

The surface stress p used in Eqs. (8) and (10) can be predicted by CET. The surface stress can be expressed as a function of the instantaneous velocity [47] as follows:

$$\frac{p}{f_c} = A' + B'\frac{v_n}{\left(f_c/\rho_t\right)^{0.5}} + C'\frac{v_n^2}{f_c/\rho_t}, \tag{11}$$

where $v_n = V\cos\theta$ is the cavity-expansion velocity at the projectile-concrete interface, V is the instantaneous projectile velocity, and θ is the angle between the normal to the nose surface and the projectile axis. The Drucker-Prager Cap yield criterion [48] and the HJC model [37,39] were used in this study. The response of concrete to the expansion of a cavity can be subdivided into four regimes: elastic, cracked, compacted, and comminuted. The Runge-Kutta method was used to solve the governing differential equations for each regime, except for the elastic and cracked regimes for which the analytical solution was provided by Satapathy [49]. According to the cavity expansion theory for compressible materials proposed by Forrestal [10], the above analysis produces a fitting curve that reflects the expansion velocity and stress in dimensionless form, giving the parameters A', B', and C'. The axial resistance on the projectile nose can also be integrated from the normal compressive stresses and the tangential stress. Thus,

$$F_{drag} = \oiint p(\sin\theta + \mu'\cos\theta)dA_s, \tag{12}$$

where μ' is the sliding friction coefficient in impact.

According to Newton's second law, the instantaneous velocity V_1 of the projectile that characterizes the start of the tunnel region and the moment t_1 can be predicted as follows:

$$\begin{cases} V_1 = \dfrac{-A_2 + \sqrt{A_2^2 - 4\left(A_3 + \frac{m}{4a}\right)\left(A_1 - \frac{mV_s^2}{4a}\right)}}{2\left(A_3 + \frac{m}{4a}\right)}, \\[2mm] t_1 = \dfrac{4a\cos^{-1}(V_1/V_s)}{\sqrt{V_s^2 - V_1^2}}, \end{cases} \tag{13}$$

where A_1, A_2, and A_3 are shape parameters of projectile nose that can be calculated by the expression (Eq. (8)) in Ref. [50].

In addition, the angle θ expresses the fact that the projectile nose profile has an effect on the force exerted on the projectile. Because of mass abrasion, the nose shape varied with penetration time. According to Eq. (12), the normal compressive stresses and the tangential stress on the projectile nose also varied with the penetration time, which indicates that the axial resistance and friction force are not constant and are related to the nose variation. Thus, the nose profile also affects the heat friction generated between the projectile and the target.

The coupled abrasion model can hence be expressed as

$$\begin{cases} \sigma_r - \sigma_\theta = g(p), \\ p = f(\mu), \\ \dfrac{p}{f_c} = A' + B' \dfrac{v_n}{(f_c/\rho_t)^{0.5}} + C' \dfrac{v_n^2}{f_c/\rho_t}, \\ E_{\text{total}} = \displaystyle\int_{t_1}^{t_e}\left[Z\dfrac{pv_r(t)}{\sigma_y(t)} + h_m \mathrm{d}A_s\right]\mathrm{d}t. \\ \sigma_y = \sigma\left[1 + C\ln\left(\dfrac{\dot{\varepsilon}}{\dot{\varepsilon}_0}\right)\right]\left[1 - \left(\dfrac{T - T_0}{T_m - T_0}\right)^m\right]. \end{cases} \tag{14}$$

The entire penetration process was divided into continuous time steps. In each time step, the temperature distribution on the projectile surface affected the yield stress of the projectile material and subsequently affected the abrasion volume because of the cutting mechanism, according to Eq. (13). Concurrently, the cutting of the projectile surface material by the aggregates determines the nose profile and the surface stresses on the projectile nose, which implies that the cutting mechanism also affects the friction heat and temperature distribution of the projectile in the next time step. Thus, the two dominant abrasion mechanisms, thermal melting and cutting by aggregates, occur simultaneously during penetration.

The evolution of the nose, DOP, and mass loss in each time step can be calculated using Eqs. (7), (8), and (10), by focusing on the thermodynamic analysis of the projectile and

ignoring the influence of the various steel projectile components. Through the above analysis, the parameters in the HJC model, Drucker-Prager Cap failure criterion, and Johnson-Cook model used in the present abrasion model are listed in Table 4. According to Refs. [45,47], $T_m = 1793$ K is the melting point of the projectile, $\lambda = 44.5$ W/(m K) is the coefficient of heat conduction, $c_p = 477$ J/(kg K) is the heat capacity of the projectile, and $C = 0.014$ and $m = 1.03$ are parameters used in the Johnson-Cook model. Finally, the ultimate DOP and mass loss of the projectile can be predicted after the normal penetration. Furthermore, the evolution of the projectile nose at various times during the penetration process can be predicted using the present model.

5. Comparing the coupled abrasion model with the experimental data and other theoretical models

5.1 Comparison of the coupled abrasion model with the experimental data

This study assumed that all the penetration trajectories were straight. Through the analysis of previous chapter, the key parameters A', B', and C' for theoretical calculation are 9.04, 0.86, and 0.72. Figure 8 shows the ultimate DOP predicted by the present model, the experimental data, and the error. Most of the prediction errors on the DOP and mass loss rate were less than 20.0 %, indicating consistency with the test data.
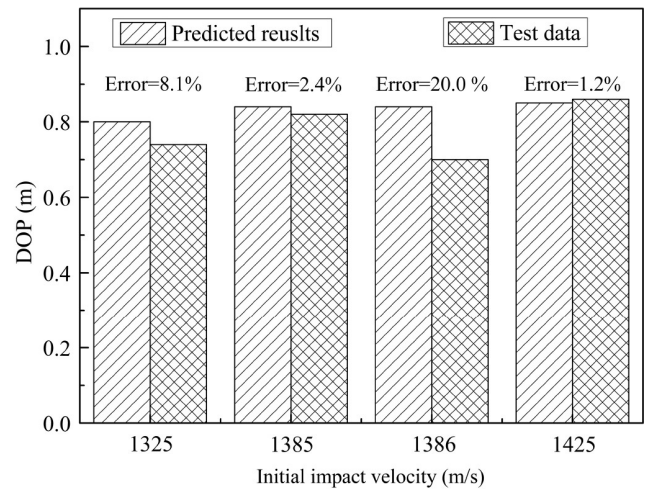
Particularly, when the initial impact velocity was

Figure 8 Comparison of theoretical model prediction of DOP with experimental results.

Table 4 Parameters in present theoretical model [39,47]

f_c (MPa)	ρ_t (kg/m³)	P_c (MPa)	P_l (MPa)	μ_c	μ_l	K_1 (GPa)	K_2 (GPa)	K_3 (GPa)
50.0	2300	16.67	0.014	0.0013	0.11	85	171	208

P_m (MPa)	$\tan\beta$	R	T_m (K)	λ (W/(m K))	c_p (J/(kg K))	C	m
496	0.67	0.91	1793	44.5	477	0.014	1.03

1386 m/s, a large deviation occurred between the prediction results of the present model and the test data. This was because concrete is an anisotropic material, and the experimental process is affected by numerous factors. The DOP results of this group test are even lower than the DOP results for the initial impact velocities of 1385 and 1325 m/s. The possible reason for this accidental error is the deflected trajectory of the projectile during the penetration experiment. Thus, the above discussion indicates that the coupled abrasion model effectively predicts the DOP and mass loss of projectiles during high-speed penetration.

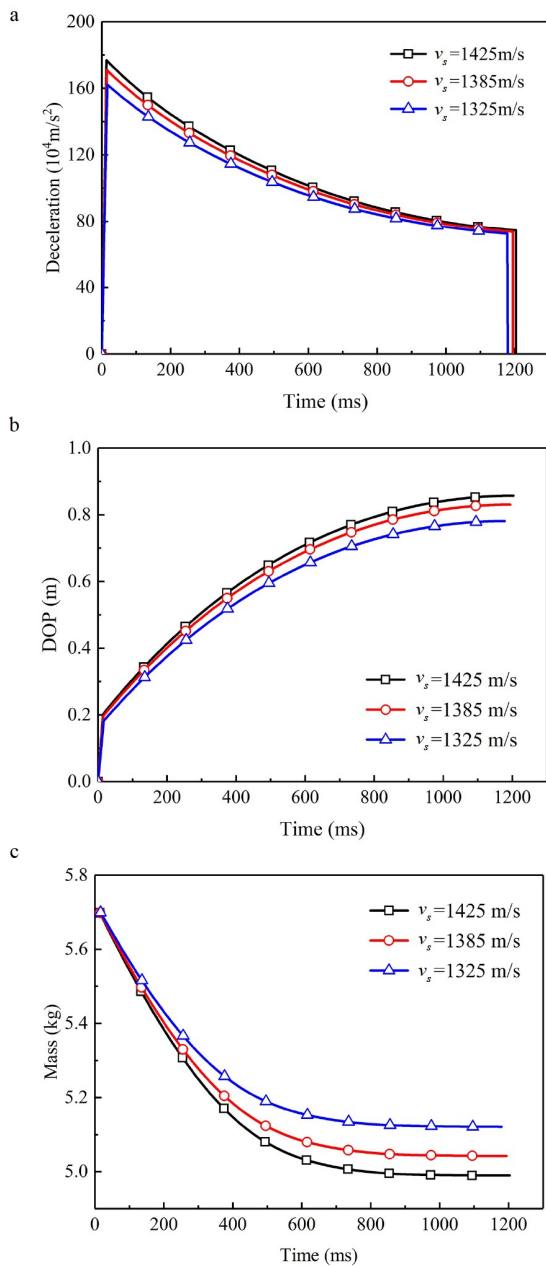Figure 9 plots the variation of the deceleration, penetration

depth, and residual mass of the projectile as functions of time during the four groups of penetration experiments. The deceleration peaks at the initial stage of penetration and decreases nonlinearly with increasing penetration time, as shown in Fig. 9a. Furthermore, Fig. 9b reveals that, in a certain velocity range, the penetration depth increases with the initial projectile impact velocity. At the initial stage of penetration, the DOP increases rapidly. As the penetration progresses, the rate of increase declines until the final penetration depth is reached. Similarly, at the initial stage of penetration, the residual projectile mass decreases rapidly. As penetration progresses, the mass decreases more slowly until the final mass loss is reached, as shown in Fig. 9c.

To further verify the validity of the proposed model, the three-dimensional (3D) geometry models of the recovered projectiles after penetration were obtained by 3D scanning, considering that the resistance of the projectile is generally not uniform under complex experimental conditions, the mass abrasion of the projectile nose may be uneven. However, the nose shape of the residual projectile after penetration, while remaining approximately ogival, is blunter than that of the pristine projectile from the 3D geometry model, which indicates that the residual projectiles did not experience structural deformation. Therefore, simplifying the 3D projectile into a two-dimensional profile is feasible for the analysis and the application of the dynamic cavity expansion theory to the present model. Figure 10a compares the projectile shape predicted by the present model and the residual projectile shape obtained from the test. The predicted nose shape is axisymmetric, whereas the nose shape of the profile of residual projectiles was not axisymmetric. During penetration, a considerable resistive force was applied on the outer surface of the projectile by the target medium. However, the force on the projectile head may not be symmetrical. Thus, the present model effectively predicts the shape
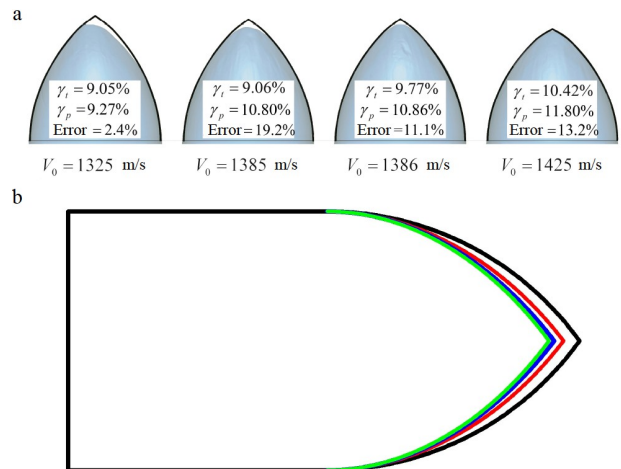

Figure 9 Variation of the projectile deceleration, penetration depth, and residual mass with penetration time. **a** Deceleration, **b** penetration depth, **c** residual mass.

Figure 10 Comparison results. **a** Comparison of the nose shape predicted by present model with test data. **b** Comparison of nose profile at different time (0, 0.25, 0.5, 0.75, 1.18 ms).

of the residual projectile after it penetrates the concrete slab.

Figure 10b shows the real-time projectile profile as it penetrates, as predicted by the present method, for an initial impact velocity of 1425 m/s. The deformation is most severe at the initial stage of penetration, which is mainly attributed to the high initial instantaneous velocity of the projectile. This generates considerable resistance on the projectile body surface, which in turn produces considerable erosion of the surface, as calculated by the erosion projectile model. The instantaneous projectile velocity decreases with increasing penetration time, which decreases the penetration resistance and abrasion. This makes the change in the projectile profile more moderate than at the initial stage of penetration.

To further verify the validity of the present model, the experimental data of projectile penetrating 62.8 MPa [27] and 58.4 MPa [20] concrete were selected for comparative analysis. The material parameters required for present theoretical calculation are listed in Tables 5 and 6. Based on cavity expansion theory, the key parameters A′, B′, and C′ of 62.8 MPa concrete are 10.9, −1.41, and 1.07, the key parameters A′, B′, and C′ of 58.4 MPa concrete are 11.1, −0.88 and 1.06. Figures 11 and 12 compare experimental data for projectiles penetrating 62.8 MPa and 58.4 MPa concrete with the calculated results of the present model. The model and experiments show good agreement.

5.2 Comparison of theoretical predictions and published experimental data

The experimental data of Forrestal et al. [20,27] on deep penetration in concrete were used to verify the accuracy of the proposed model, such as Guo et al. [24] and Chen et al. [35]. Therefore, the four-set penetration test results in Ref. [20] were also collected in this study.

Table 7 first compares the mass-loss rates predicted by various models with the test data, and second the projectile nose shape after penetration. Guo's model underestimates the mass loss of the projectile at low speed. The corresponding error is 28.0% for an initial impact velocity of 651 m/s. This
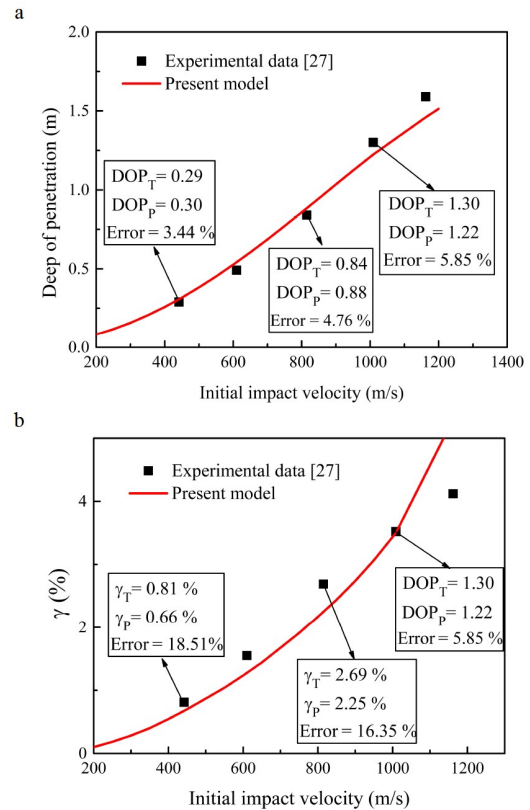

Figure 11 Comparison results of projectiles penetrating 62.8 MPa concrete. **a** Penetration depth, **b** mass abrasion.

is attributed to the single abrasion mechanism of the model. On the other hand, Chen's model overestimates the mass loss of the projectile during high-speed penetration. Furthermore, based on Silling's study [23], Chen introduced an experimental fitting parameter to modify the theoretical model. The modified model provides accurate predictions for initial impact velocities below 1000 m/s, but its application to high-speed penetration is limited. In contrast to these two abrasion models, the error between the present model and experimental data is less than 5%. Table 5 also compares the projectile nose shape after penetration for various initial impact velocities. At low initial impact velocities, the nose shapes predicted by the various theoretical models are similar and consistent with the nose shape of the residual projectiles. With increasing initial impact velocity, Chen's predicted projectile nose shape after penetration into the concrete slab is excessively blunt compared with that of the test. This discrepancy is mainly attributed to the fact that Chen simulated nose blunting by reducing its CRH value. Chen predicted a hemispherical nose shape when the mass loss was high. Conversely, Guo predicted an excessively sharp nose shape after penetration into the concrete slab, when compared with that of the test for a high initial impact velocity. However, the comparison results reveal that the proposed model predicts the projectile mass loss accurately, especially
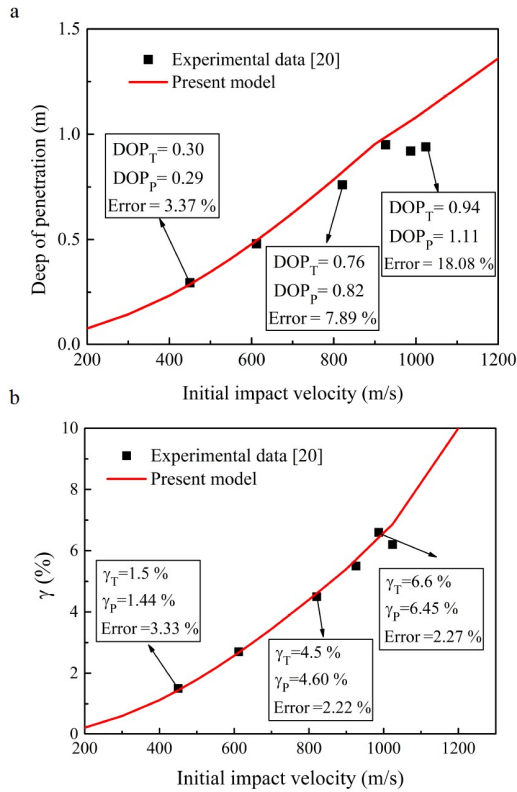
Table 5 Parameters of 62.8 MPa concrete in present theoretical model [47,48]

f_c (MPa)	ρ_t (kg/m³)	P_c (MPa)	P_l (MPa)	μ_c	μ_l
62.8	2300	20.93	800	0.0013	0.11

K_1 (GPa)	K_2 (GPa)	K_3 (GPa)	P_m (MPa)	$\tan\beta$	R
85	171	208	469	0.67	0.91

Table 6 Parameters of 58.4 MPa concrete in present theoretical model [47,48]

f_c (MPa)	ρ_t (kg/m³)	P_c (MPa)	P_l (MPa)	μ_c	μ_l
58.4	2320	19.47	800	0.0013	0.11

| K_1 (GPa)	K_2 (GPa)	K_3 (GPa)	P_m (MPa)	$\tan\beta$	R
85	171	208	471	0.67	0.91

Figure 12 Comparing predictions and experimental results for projectiles penetrating 58.4 MPa concrete. **a** Penetration depth, **b** mass abrasion.

Table 7 Comparison between the calculated results and experimental results of different models

	651 m/s	821 m/s	900 m/s	1009 m/s
Guo's model (%)	2.23	4.20	5.30	6.50
Chen's model (%)	2.96	4.52	4.72	7.00
Present model (%)	2.98	4.49	5.51	6.44
Test data (%)	3.1	4.4	5.4	6.4
Comparison of projectile head shape				
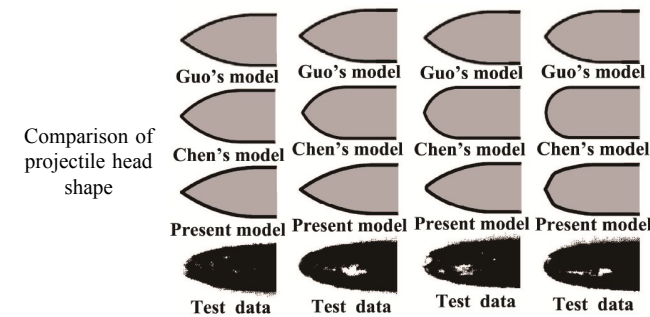
the penetration performance at high initial impact velocities.

The theoretical model proposed in this paper is certainly suitable for high-speed and low-speed penetration, but not for ultra-high-speed penetration ($V_s > 1500$ m/s). This is because the projectile maintains its structural integrity during high-speed penetration and does not enter a semi-fluid state. Therefore, this model applies to the high-speed penetration speed range where melting and cutting are the main abrasion mechanisms. It can also be used for low-speed penetration. However, it is unsuitable for ultra-high-speed penetration, where the structural integrity of the projectile is compromised, and melting and cutting are no longer the dominant abrasion mechanisms.

6. Conclusion

Mass abrasion has an evident effect on the penetration performance of projectiles, and the microscopic observation of residual projectiles is critical for understanding the relevant mechanisms. We conducted experimental studies on 100.0-mm-diameter projectiles penetrating 50.0 MPa concrete targets at a high initial impact velocity to investigate the mechanisms of mass abrasion. The residual projectiles were recovered after penetration, and the samples sectioned at various locations from the nose of the residual projectile were observed from multiple angles at the microscopic scale.

Thus, the mechanism of mass erosion during high-speed projectile penetration can be investigated by a microscopic observation of residual projectiles. Two typical micromorphologies were observed: (1) a continuous HAZ of varying thickness was distributed on the cross and longitudinal sections of the projectile surface layer after penetration, which confirmed the melting of part of the outer projectile surface; (2) the V-shaped outer surface profile of the longitudinal section of the projectile surface layer indicated that some of the material on the projectile surface was cut by hard particles and aggregates in concrete.

The above microscopic observation and the comparison between experimental data and previous models reinforce the conclusions that the mass abrasion of projectiles during high-speed penetration cannot be ignored, and that mass abrasion involves multiple mechanisms acting simultaneously. Models based on a single abrasion mechanism yield inaccurate predictions of projectile abrasion during high-speed penetration. Therefore, a projectile penetration model based on the cavity expansion theory was established by considering the two main mass-loss mechanisms observed in the microscopic tests: thermal melting and cutting. The resulting theoretical predictions of the penetration depth, mass-loss rate, and change of projectile head were consistent with test data provided in this study and in previous publications. Their comparisons reveal that the proposed model predicts the mass loss of the projectile accurately, especially the penetration performance for high initial impact velocities.

Author contributions *Jianguo Ning designed the research. Zhao Li and Xiangzhao Xu wrote the first draft of the manuscript. Zhao Li and Xiangzhao Xu set up the experiment set-up and processed the experiment data. Huilan Ren and Xiangzhao Xu helped organize the manuscript. Jianguo Ning, Huilan Ren, Zhao Li and Xiangzhao Xu revised and edited the final version.*

1. J. Ning, F. Meng, T. Ma, and X. Xu, Failure analysis of reinforced concrete slab under impact loading using a novel numerical method, Int. J. Impact Eng. **144**, 103647 (2020).
2. C. G. Chai, A. G. Pi, Q. M. Li, and F. L. Huang, Similarities in the penetration depth of concrete impacted by rigid projectiles, Acta Mech. Sin. **36**, 1294 (2020).
3. D. Yankelevsky, and V. Feldgun, The embedment of a high velocity rigid ogive nose projectile into a concrete target, Int. J. Impact Eng. **144**, 103631 (2020).
4. X. Zhang, H. Wu, S. Zhang, and F. L. Huang, Projectile penetration of reinforced concrete considering the effect of steel reinforcement: Experimental study and theoretical analysis, Int. J. Impact Eng. **144**, 103653 (2020).
5. J. Zhang, W. Chen, H. Hao, Z. Wang, Z. Wang, and X. Shu, Performance of concrete targets mixed with coarse aggregates against rigid projectile impact, Int. J. Impact Eng. **141**, 103565 (2020).
6. X. Huang, X. Kong, J. Hu, X. Zhang, Z. Zhang, and Q. Fang, The influence of free water content on ballistic performances of concrete targets, Int. J. Impact Eng. **139**, 103530 (2020).
7. D. Z. Yankelevsky, and V. R. Feldgun, Issues in modelling the penetration of thick targets by rigid long rods, Int. J. Impact Eng. **137**, 103474 (2020).
8. C. Liu, X. Zhang, H. Chen, J. Wang, H. Wei, and W. Xiong, Experimental and theoretical study on steel long-rod projectile penetration into concrete targets with elevated impact velocities, Int. J. Impact Eng. **138**, 103482 (2020).
9. D. Jiang, W. Q. Shi, R. Y. Huang, Z. L. Liu, M. R. Li, B. W. Qian, and G. Zhou, Scale effects and similarity laws on high/hypervelocity impact penetration, Sci. Sin.-Phys. Mech. Astron. **51**, 104710 (2021).
10. M. J. Forrestal, and D. Y. Tzou, A spherical cavity-expansion penetration model for concrete targets, Int. J. Solids Struct. **34**, 4127 (1997).
11. M. J. Forrestal, B. S. Altman, J. D. Cargile, and S. J. Hanchak, An empirical equation for penetration depth of ogive-nose projectiles into concrete targets, Int. J. Impact Eng. **15**, 395 (1994).
12. X. Zhang, R. Cao, D. Tan, and B. Wang, Different scale experiments of high velocity penetration with concrete targets, J. Appl. Mech. **80**, 031802 (2013).
13. J. Ning, W. Song, and G. Yang, Failure analysis of plastic spherical shells impacted by a projectile, Int. J. Impact Eng. **32**, 1464 (2006).
14. L. Guo, Y. He, X. F. Zhang, C. X. Pang, L. Qiao, and Z. W. Guan, Study mass loss at microscopic scale for a projectile penetration into concrete, Int. J. Impact Eng. **72**, 17 (2014).
15. L. L. He, X. W. Chen, and Z. H. Wang, Study on the penetration performance of concept projectile for high-speed penetration (CPHP), Int. J. Impact Eng. **94**, 1 (2016).
16. H. J. Wu, F. L. Huang, Y. N. Wang, and Z. P. Duan, Experimental investigation on projectile nose eroding effect of high-velocity penetration into concrete, Acta Armamentarii **33**, 48 (2012).
17. H. Dong, Z. Liu, H. Wu, X. Gao, A. Pi, and F. Huang, Study on penetration characteristics of high-speed elliptical cross-sectional projectiles into concrete, Int. J. Impact Eng. **132**, 103311 (2020).
18. J. Ning, H. Ren, T. Guo, and P. Li, Dynamic response of alumina ceramics impacted by long tungsten projectile, Int. J. Impact Eng. **62**, 60 (2013).
19. H. Wu, X. W. Chen, Q. Fang, and L. L. He, Stability analyses of the mass abrasive projectile high-speed penetrating into concrete target. Part II: Structural stability analyses, Acta Mech. Sin. **30**, 943 (2014).
20. M. J. Forrestal, D. J. Frew, S. J. Hanchak, and N. S. Brar, Penetration of grout and concrete targets with ogive-nose steel projectiles, Int. J. Impact Eng. **18**, 465 (1996).
21. S. E. Jones, J. C. Foster, O. A. Toness, R. J. DeAngelis, and W. K. Rule, in An estimate for mass loss from high velocity steel penetrators: Proceedings of the ASME PVP-435 Conference on Thermal-Hydraulic Problems, (ASME, New York, 2002), pp. 227-237.
22. X. Xu, T. Ma, and J. Ning, Failure analytical model of reinforced concrete slab under impact loading, Constr. Building Mater. **223**, 679 (2019).
23. S. A. Silling, and M. J. Forrestal, Mass loss from abrasion on ogive-nose steel projectiles that penetrate concrete targets, Int. J. Impact Eng. **34**, 1814 (2007).
24. L. Guo, Y. He, X. Zhang, Y. He, J. Deng, and Z. Guan, Thermal-mechanical analysis on the mass loss of high-speed projectiles penetrating concrete targets, Eur. J. Mech.-A Solids **65**, 159 (2017).
25. O. Hao, and X. Chen, Modeling on mass loss and nose blunting of high-speed penetrator into concrete target, Int. J. Prot. Struct. **10**, 3 (2019).
26. X. Xu, T. Ma, H. Liu, and J. Ning, A three-dimensional coupled Euler-PIC method for penetration problems, Int. J. Numer. Methods Eng. **119**, 737 (2019).
27. D. J. Frew, S. J. Hanchak, M. L. Green, and M. J. Forrestal, Penetration of concrete targets with ogive-nose steel rods, Int. J. Impact Eng. **21**, 489 (1998).
28. J. Feng, M. Song, W. Sun, and Z. P. Duan, Experimental investigation on projectile nose eroding effect of high-velocity penetration into concrete, ACTA Armamentarii **122**, 305 (2018).
29. L. Guo, Y. He, N. S. Zhang, C. X. Pang, and H. Zheng, On the mass loss of a projectile based on the Archard theory, Explosion Shock Waves **34**, 622 (2014).
30. L. L. He, X. W. Chen, and X. He, Parametric study on mass loss of penetrators, Acta Mech. Sin. **26**, 585 (2010).
31. H. Yang, X. Jin, J. Zhang, Z. Wang, and Z. Wang, Analysis on Mass loss of different sized projectiles penetrating into concrete targets, Int. J. Mech. Sci. **131-132**, 683 (2017).
32. H. M. Wen, Y. Yang, and T. He, Effects of abrasion on the penetration of ogival-nosed projectiles into concrete targets, Lat. Am. J. Solids Struct. **7**, 413 (2010).
33. L. L. He, X. W. Chen, and Y. M. Xia, Representation of nose blunting of projectile into concrete target and two reduction suggestions, Int. J. Impact Eng. **74**, 132 (2014).
34. J. Zhao, X. W. Chen, F. N. Jin, and Y. Xu, Depth of penetration of high-speed penetrator with including the effect of mass abrasion, Int. J. Impact Eng. **37**, 971 (2010).
35. X. W. Chen, L. L. He, and S. Q. Yang, Modeling on mass abrasion of kinetic energy penetrator, Eur. J. Mech.-A Solids **29**, 7 (2010).
36. R. N. Davis, A. M. Neely, and S. E. Jones, Mass loss and blunting during high-speed penetration, Proc. Inst. Mech. Eng. Part C-J. Mech. Eng. Sci. **218**, 1053 (2004).
37. G. M. Ren, H. Wu, Q. Fang, and X. Z. Kong, Parameters of Holmquist-Johnson-Cook model for high-strength concrete-like materials under projectile impact, Int. J. Prot. Struct. **8**, 352 (2017).
38. W. Wan, J. Yang, G. Xu, and Y. Liu, Determination and evaluation of holmquist-johnson-cook constitutive model parameters for ultra-high-performance concrete with steel fibers, Int. J. Impact Eng. **156**, 103966 (2021).
39. T. J. Holmquist, and G. R. Johnson, A computational constitutive model for glass subjected to large strains, high strain rates and high pressures, J. Appl. Mech. **78**, 051003 (2011).
40. S. J. Hanchak, M. J. Forrestal, E. R. Young, and J. Q. Ehrgott, Perforation of concrete slabs with 48 MPa (7 ksi) and 140 MPa (20 ksi) unconfined compressive strengths, Int. J. Impact Eng. **12**, 1 (1992).
41. N. Gebbeken, S. Greulich, and A. Pietzsch, Hugoniot properties for concrete determined by full-scale detonation experiments and flyer-plate-impact tests, Int. J. Impact Eng. **32**, 2017 (2006).
42. M. J. Forrestal, D. J. Frew, J. P. Hickerson, and T. A. Rohwer, Penetration of concrete targets with deceleration-time measurements, Int. J. Impact Eng. **28**, 479 (2003).
43. V. K. Luk, and M. J. Forrestal, Penetration into semi-infinite reinforced-concrete targets with spherical and ogival nose projectiles,

J. Ning, *et al. Acta Mech. Sin.*, Vol. 38, 121597 (2022)

121597-14

Int. J. Impact Eng. **6**, 291 (1987).

44 E. Rabinowicz, L. A. Dunn, and P. G. Russell, A study of abrasive wear under three-body conditions, Wear **4**, 345 (1961).

45 G. R. Speich, and H Warlimont, Yield strength and transformation substructure of low-carbon martensite, Iron Steel Inst. **206**, 385 (1968).

46 W. H Cook, and G. R Johnson, in A constitutive model and data for metals subjected to large strains, high strain rates and high temperatures: Proceedings of the 7th International Symposium on Ballistics, Netherlands, 1983, pp. 541-547.

47 X. Wang, Effects of constitutive parameters on adiabatic shear loca-

lization for ductile metal based on JOHNSON-COOK and gradient plasticity models, Trans. Nonferrous Met. Soc. China **16**, 1362 (2006).

48 J. Feng, W. Li, X. Wang, M. Song, H. Ren, and W. Li, Dynamic spherical cavity expansion analysis of rate-dependent concrete material with scale effect, Int. J. Impact Eng. **84**, 24 (2015).

49 S. Satapathy, Dynamic spherical cavity expansion in brittle ceramics, Int. J. Solids Struct. **38**, 5833 (2015).

50 H. J. Wu, F. L. Huang, Y. N. Wang, Z. P. Duan, and Y. Shan, Mass loss and nose shape change on ogive-nose steel projectiles during concrete penetration, Int. J. Nonlinear Sci. Numer. Simul. **13**, 273 (2012).

高速侵彻混凝土靶过程中耦合融化与切削机制的弹体质量侵蚀模型

宁建国, 任会兰, 李钊, 许香照

摘要 本文开展了初始撞击速度为1325.0 m/s~1425.0 m/s范围内的卵形弹体侵彻混凝土试验. 获取了弹体的侵彻深度及质量损失等试验数据, 并对侵彻试验后的剩余弹体进行了回收. 通过对剩余弹体不同部位切片和外表面的微观观测, 分析了弹体质量侵蚀的内在机理. 结果表明, 卵形弹体高速侵彻混凝土过程中的质量侵蚀现象是多种机制耦合造成的. 基于空腔膨胀理论和微观试验中观测得到的两种主要侵蚀机理, 建立了计及质量侵蚀的弹体侵彻理论模型. 理论模型预测的弹体侵彻深度、质量损失率和弹头形状变化与本文试验及前人试验结果吻合较好.